

MICROSTRUCTURE AND MECHANICAL PROPERTIES OF WE43 ALLOY
PRODUCED VIA ADDITIVE FRICTION STIR TECHNOLOGY

Jacob Rollie Calvert

Thesis submitted to the faculty of the Virginia Polytechnic Institute and State University
in partial fulfillment of the requirements for the degree of

Master of Science

In

Material Science and Engineering

William T. Reynolds Jr

Christopher B. Williams

Kumar Kandasamy

6/29/2015

Blacksburg, VA

Keywords:

Additive, Friction Stir, Manufacturing, Magnesium, WE43

MICROSTRUCTURE AND MECHANICAL PROPERTIES OF WE43 ALLOY PRODUCED VIA ADDITIVE FRICTION STIR TECHNOLOGY

Jacob Rollie Calvert

ABSTRACT

In an effort to save weight, transportation and aerospace industries have increasingly investigated magnesium alloys because of their high strength-to-weight ratio. Further efforts to save on material use and machining time have focused on the use of additive manufacturing. However, anisotropic properties can be caused by both the HCP structure of magnesium alloys as well as by layered effects left by typical additive manufacturing processes. Additive Friction Stir (AFS) is a relatively new additive manufacturing technology that yields wrought microstructure with isotropic properties. In this study, Additive Friction Stir (AFS) fabrication was used to fabricate WE43 magnesium alloy, with both atomized powder and rolled plate as filler material, into multilayered structures. It was found that the WE43 alloy made by AFS exhibited nearly isotropic tensile properties. With aging these properties exceeded the base material in the T5 condition. The toughness measured by Charpy impact testing also showed an increase over the base material. The relationships among tensile properties, Vickers microhardness, impact toughness, microstructure and thermal history are developed and discussed.

Acknowledgements

I would like to gratefully acknowledge the contributions and support of Kevin Doherty and the U.S. Army Research Lab.

This work would not have been possible without the support of Aeroprobe Corporation and specifically the hard work and guidance of the Additive Friction Stir team.

I am also very appreciative of the staff at Virginia Tech, and especially grateful to the staff and students in the Material Science Department and the CRC.

Thanks to my wife, my friends, and my family for their love and encouragement.

Table of Contents

Acknowledgements.....	iii
Table of Contents.....	iv
List of Figures	v
List of Tables	vi
Introduction	1
Experimental Details.....	2
Results.....	4
Deposition.....	4
Microstructure	4
Tensile Results.....	6
Vickers Microhardness Results	8
Charpy Impact Test Results.....	9
Thermal Profile.....	12
DISCUSSION.....	13
CONCLUSIONS.....	15
References	16

List of Figures

Figure 1: Additive Friction Stir process and sample Aluminum deposition.....	2
Figure 2: XZ Cross section and sample locations.....	3
Figure 3: Micrographs of (a) WE43 -100/+325 atomized powder partially consolidated inside the tool, (b) consolidated powder exiting the tool and microstructures from Part 1 (c) and Part 2 (d).....	4
Figure 4: Micrographs of (a) WE43-T5 rolled plate used for feed, and Part 3 from (b) longitudinal and (c) transverse directions	5
Figure 5: Tensile results by sample orientation for (a) Ultimate Strength, (b) Yield, and (c) Elongation.....	6
Figure 6: Typical stress-strain curves for (a) different sample orientations of Part 2, and (b) the ZY orientation in the base and Parts 1, 2, and 3 as deposited.....	7
Figure 7: XY tensile results by layer for (a) Part 2 and (b) Part 3	8
Figure 8: Vickers microhardness profiles of as deposited (a) Part 1, (b) Part 2, and (c) Part 3. ...	9
Figure 9: Representative fracture surface topography for (a) WE43-T5 plate, (b) Part 1, (c) Part 2 and (d) Part 3.....	10
Figure 10: WE43-T5 fractograph (a) and representative microstructure (b) of fracture surface.	11
Figure 11: Fractographs from Charpy impact samples of (a) Part 1, (b) Part 2 and from (c) transverse tensile sample of Part 2. Representative microstructure (d) from Part 1	11
Figure 12: Part 3 Charpy impact sample fractograph (a), macrograph (b), and microstructure (c).	12
Figure 13: Thermal profile of Part 1 substrate during deposition.....	12
Figure 14: Hall-Petch relationship of deposit and substrate interface.	14

List of Tables

Table 1: Vickers Microhardness Results.....	8
Table 2: Charpy Impact Results.....	9

Introduction

The high specific strength, or strength to weight ratio, of magnesium alloys has made them more desirable for the transportation industry where attempts are being made to lighten structures as a way of increasing fuel economy.¹ This is made difficult by the low dynamic strength exhibited in magnesium alloys at room temperature caused by their low ductility and fracture toughness resulting from the limited availability of slip systems in HCP structures. Increases in strength and ductility have been shown through processes of grain refinement,² which improves the ductility of magnesium alloys by activating more slip systems and by decreasing the common tendency for slip along the basal and prismatic planes.³ Grain refinement can be achieved by processing methods that use severe plastic deformation⁴, such as rolling, forging, and extrusion. These techniques tend to align the crystallography along the direction of material flow during the deformation process giving higher strength in that direction, but also accentuate the anisotropic behavior⁵ of magnesium and result in lower strength and ductility in the directions perpendicular to flow.

In order to promote grain refinement, and to reduce texture associated with processing, modern magnesium alloys now include rare earth elements. The magnesium alloy WE43 is one these new alloys which contains the rare earth elements Neodymium (Nd) to reduce texture by encouraging recrystallization of random grain orientations through particle-stimulated nucleation,⁶ and Yttrium (Y) which allows for solid-solution strengthening and precipitation hardening.⁷ With a nominal composition of Mg, 4 wt% Y, 2.3 wt% Nd, 1 wt% other rare earth and 0.6 wt% Zr,⁸ this alloy has been shown to achieve high tensile strength and ductility with thermo-mechanical treatments.⁹

Additive Manufacturing allows complex parts to be created with little or no post machining. This saves both material and machining expenses, improving the important buy-to-fly ratio. However, a successful model for the additive manufacturing of magnesium that yields an isotropic microstructure has yet to be shown. Phase transformation processes using lasers or an electron beam are bound to suffer the same drawbacks as their joining precursors. Mainly, the high temperatures and gradients lead to rapid grain growth, stress concentrations, and typical cast properties in Electron Beam Welding¹⁰ and Selective Laser Melting¹¹. Solid-state powder processes have difficulty reaching full density, and require secondary densification processes such as hot isostatic pressing.¹² Solid state joining processes converted to additive manufacturing, including ultrasonic consolidation¹³ and layered friction stir welding¹⁴, require machining between each successive layer to provide good contact surfaces and tend to leave behind layered microstructures.

Additive Friction Stir (AFS) is a solid state manufacturing process that produces near-net shape metallic parts through direct deposition. The method utilizes pressure from a rotating non-consumable tool to generate heat and plastic deformation while material is added through its center. Similar to Friction Stir Processing, the direction of the material flow is randomized by the moving tool, so the process has the potential to reduce grain size, increase homogeneity, and lower or eliminate porosity.¹⁵ Individual layers can be made with overlapping tracks, and after depositing a full layer of the desired geometry, the tool is raised and the next layer is deposited.

Through the process, the filler material is forced into the previous layer creating diffuse layers with superior bond strength. A schematic of the process is shown in Figure 1, along with a sample deposition where material is being added onto the previous 12 layers of Al 6061.

While similar processes have shown good results for the additive manufacture of magnesium alloys¹⁴, the results have yet to achieve full isotropy. This study was initiated to: (a) assess the extent to which the AFS process could reduce mechanical anisotropy in the deposited material, (b) evaluate the mechanical properties of the deposited material relative to the base plate, and (c), identify AFS process conditions that with post processing heat treatment could exceed the forged properties of WE43 in the T5 condition. In this study, the properties of AFS deposited WE43 alloy from atomized powder filler stock and WE43 rolled plate in the T5 condition filler stock are reported related to the thermal history of the depositions. Specifically, the isotropic properties that can be achieved through the rapid cooling of multi-layered depositions made from both filler materials. Uniaxial tensile, Vickers microhardness, and Charpy impact data are compared and contrasted with base WE43 in the T5 condition.

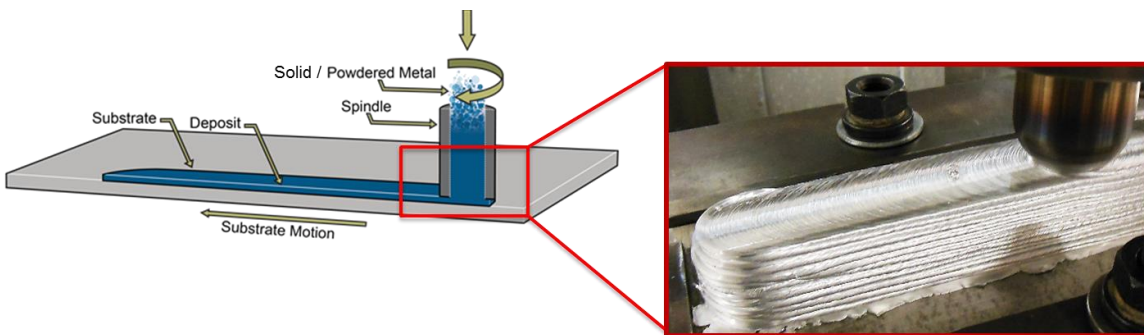


Figure 1: Additive Friction Stir process and sample Aluminum deposition

Experimental Details

Three sample parts (designated Part 1, 2, and 3) were deposited via the additive friction stir process onto 8mm thick rolled WE43-T5 plate substrates. During the AFS process, the base of the substrate was water cooled continuously. Part 1 was fabricated with -100/+325 atomized WE43 magnesium alloy powder with a tool rotation speed of 450 RPM and traveling speed of 127 mm (5 in) per minute. Four deposition and cooling cycles were used, where the part was cooled by the water-cooling plate. Part 2 was fabricated using the same parameters, except that liquid nitrogen was sprayed onto the sides of the part during deposition, to act as fast cooling to prevent grain growth, and cooling cycles were not used. At the end of the fabrication of Part 1 and 2, the tool was raised and allowed to continue to extrude consolidated powder. This consolidation, along with consolidated material left inside the tool was saved for microstructural analysis. Part 3 was fabricated with feed rods cut from the WE43-T5 rolled plate. As a result, the process required re-loading feedstock after two layers. A higher tool rotation speed of 800 RPM was used to compensate for the larger feed material grain size. A traveling speed of 102 mm (4 in) per minute was used to deposit 0.76 mm (0.03 in) thick layers. Liquid nitrogen was again used to cool the part during deposition.

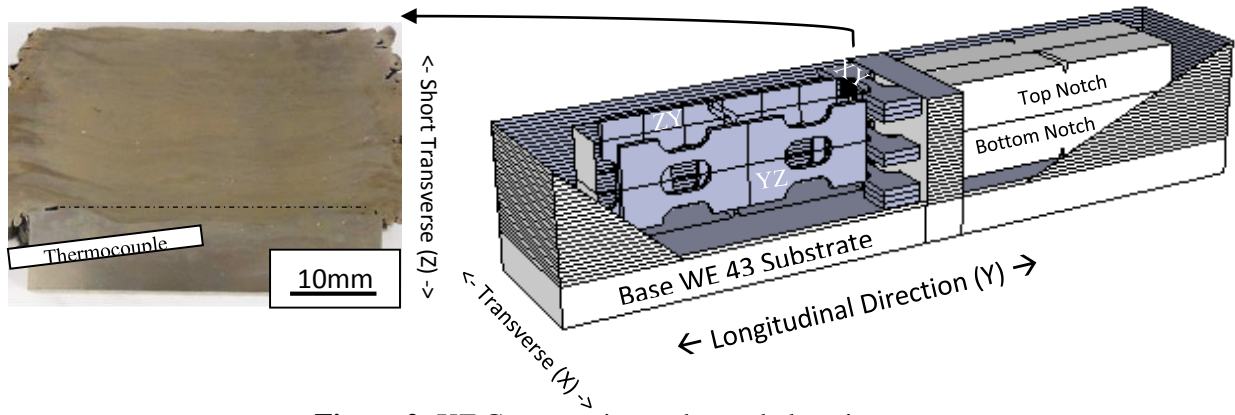


Figure 2: XZ Cross section and sample locations.

In order to determine microstructure of the deposits, an XZ cross section was milled from the center of each. YZ cross-sections were taken from the Charpy samples as well. For comparison to initial microstructure, cross sections were also taken from the consolidated powder extruded from the tool, the consolidated powder left in the tool, and from the WE43-T5 stock used for feed material in deposit 3. Samples were polished to 0.05 micron, and etched with a solution of 10 ml acetic acid, 4.2 g Picric acid, 10 ml of water, and 70 ml Ethanol. Grain size measurements were made by the linear line intercept method.

For mechanical property testing, samples were taken from multiple locations and directions throughout the deposits as shown in Figure 2. Miniaturized dogbone tensile samples with a 10 mm (0.39 in) gauge length and a 2.5 mm (0.1 in) gauge width were milled from the test block with a wire EDM in all three axial directions. XY (transverse) tensile samples were sectioned horizontally from the middle of the block, while ZY (short transverse) and YX (longitudinal) tensile samples were taken from 1mm vertical strips cut from along the side of Charpy samples as shown in Figure 2. For better comparison to the heat treated base material, extra XY and ZY tensile samples were taken from Part 2 and Part 3 and aged at 180° C. Tensile samples were then ground to a final thickness of ~1 mm (0.04 in) and polished with 600 grit emery paper. Tensile tests were run on an Instron Model 1125 with a strain rate of 1×10^{-3} /s. ASTM standard E 23 Charpy Impact samples were EDM wire milled from the deposited test bar with their notch located at the top of the deposit the bottom, or the side as shown in Figure 2. Impact testing was done on a Tinius Olson Model 84 Universal Impact Tester with 300 ft·lb force and compared with samples cut from the base plate (WE43-T5). The XZ cross-section for microstructural analysis was also used for Vickers microhardness analysis on a LECO AMH43 using a 200g load for 12 seconds.

To understand the fracture mechanisms, metallographic inspection was performed on etched cross sections of tensile and impact fracture surfaces. Fractographs from the tensile and impact fracture surfaces were gathered using a FEI Quanta 600 FEG SEM.

Thermocouples were embedded in the substrate of Part 1 before deposition in order to capture the thermal history of the part during processing. The transverse cross section in Figure 2 shows the relative position of the thermocouples.

Results

Deposition

Each layer of the deposition was observed, and no major voids were noticed. Further, no voids were noticed during the milling or preparation of test samples. The deposited layers had uniform thickness, with fairly consistent flashing (excess material left on the edges of the stir by the rotating tool). The bottom edges of the initially flat substrates had little to no curvature to them, indicating little deformation due to residual stresses in the samples. Macrographs of the part cross-sections, similar to Part 1 seen in Figure 2, also revealed no major voids or defects. The layer overlap can also be seen by the depth that the material plunged into the substrate. This is illustrated in Figure 2 by the dark material that is mixed below the dashed substrate line and lies just above the thermocouple.

Microstructure

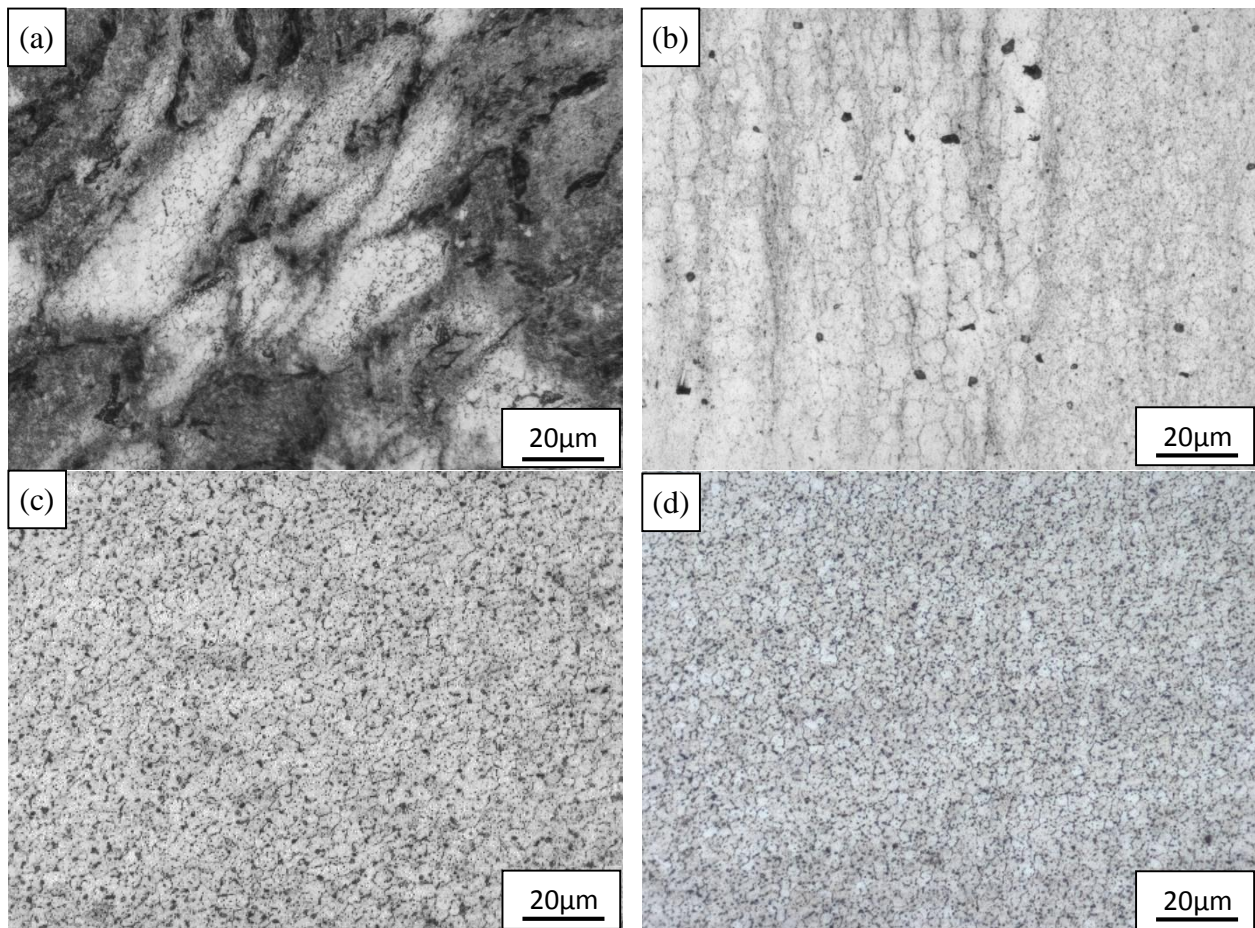


Figure 3: Micrographs of (a) WE43 -100/+325 atomized powder partially consolidated inside the tool, (b) consolidated powder exiting the tool and microstructures from Part 1 (c) and Part 2 (d).

Figure 3 displays the microstructural evolution of Part 1 and Part 2. The -100/+325 atomized powder is consolidated inside the tool (a), and consolidated, though not fully dense, material (b) is added to the deposition. Average grain size of the consolidated powder was not determined,

but grains could reach up to 10 μm in diameter. Parts 1 and 2 showed obvious grain refinement and homogenization with common grain sizes between 2 and 4 μm . Few voids could be seen in the un-etched micrographs.

Parts 1 and 2, seen in Figure 3c and d, displayed a homogeneous equiaxed fine grain microstructure. There was no obvious aspect ratio or layer interface to indicate the build direction of the part. However, both parts showed slight changes in average grain size with height. For Part 1 the average grain size was 2.5 μm at the top and bottom of the deposition and 3.2 μm in the middle. The average grain size and range for Part 2 were both smaller, with an average grain size of 2.0 μm near the top of the sample and 2.4 μm near the bottom.

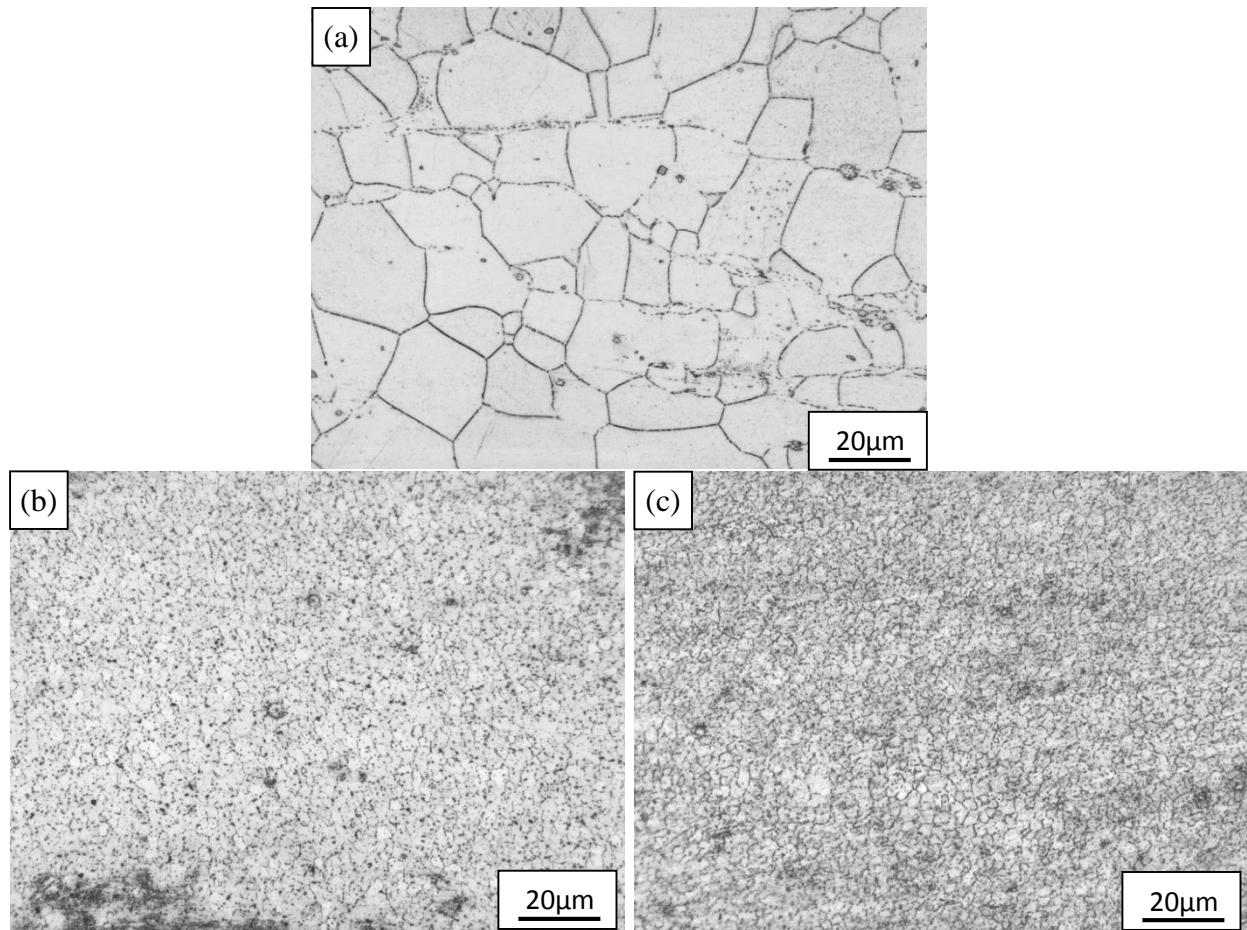


Figure 4: Micrographs of (a) WE43-T5 rolled plate used for feed, and Part 3 from (b) longitudinal and (c) transverse directions.

The microstructural evolution of Part 3 is seen in Figure 4, with the filler material (a) and the final part (b and c). The filler material has an inhomogeneous grain structure with an average grain size of 15 μm with grains as large as 60 μm in diameter. The part showed a fairly consistent fine grain microstructure throughout, with the grain size gradually increasing from 2.2 μm at the top of the sample to 2.4 μm at the bottom. However, there were several locations within the cross section where small bands of grains were not as refined as the others, as seen in the lower left corner of Figure 4c.

Tensile Results

Figure 5 displays the results for the WE43-T5 substrate, all three test parts as deposited, and Parts 2 and 3 after aging at 180 °C for 44hrs. Results are displayed for each of the three sample orientations by (a) ultimate tensile strength, (b) 0.2% yield stress, and (c) elongation to fracture. These charts quickly reveal the highest overall values by height and degree of isotropy by the change between sample directions.

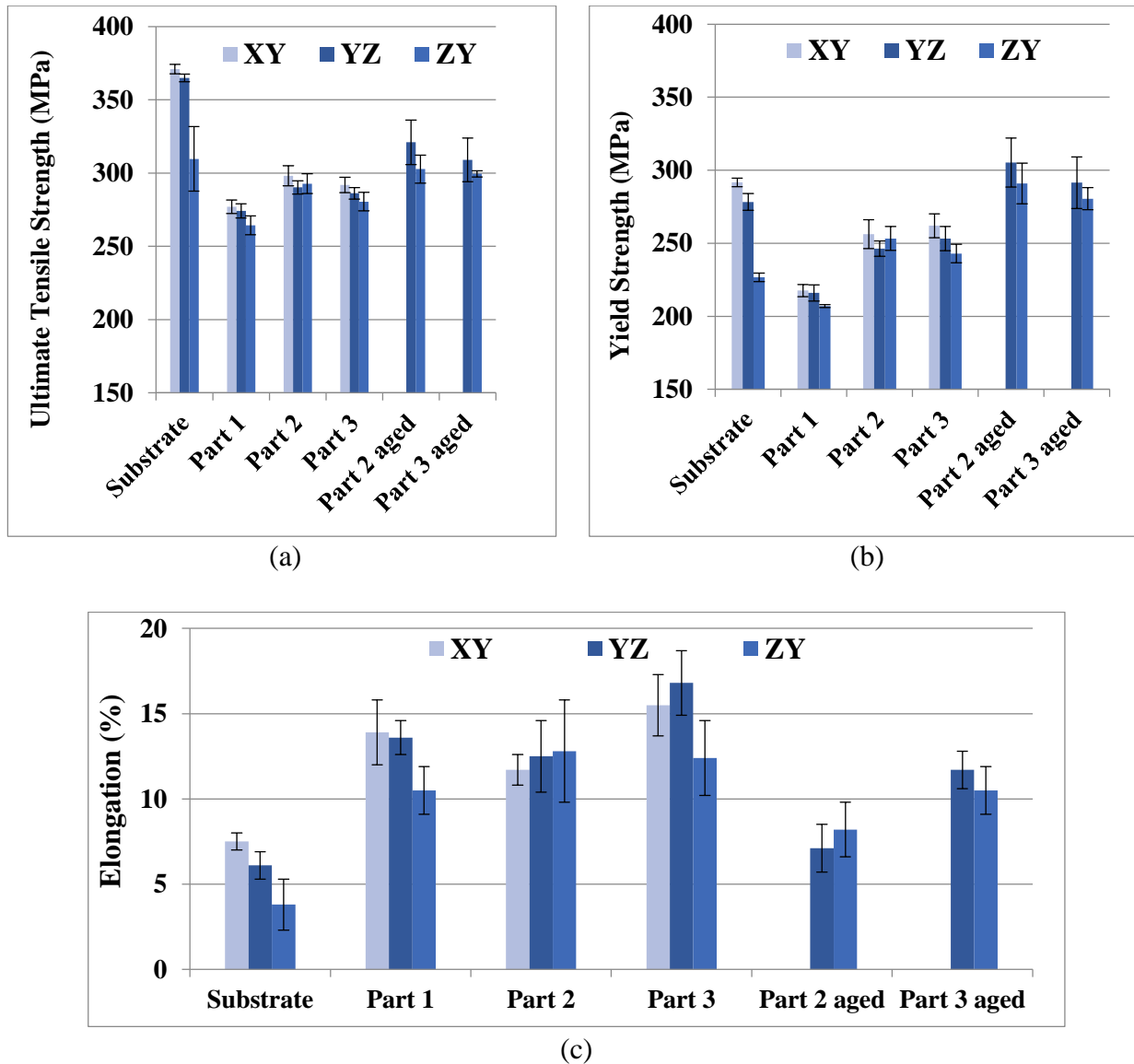


Figure 5: Tensile results by sample orientation for (a) Ultimate Strength, (b) Yield, and (c) Elongation.

The WE43-T5 substrate and filler material had high tensile and yield strength in the XY (rolling) and YX directions, but much less strength and consistency in the ZY (through thickness)

direction. It had the lowest ductility, which was heavily affected by orientation, decreasing dramatically in the ZY direction.

Part 1 increased in isotropy and ductility over the base material, but the yield and ultimate tensile strengths dropped significantly in the XY and YZ orientations. Part 2 had similar ductility, and an increase in tensile and yield strength over Part 1, but still had lower ultimate tensile and yield than the base material. Part 3 had an increase in ductility over Part 1 and 2, with yield and tensile strengths similar to Part 2. Part 2 and 3 in the aged condition had a marginally higher ultimate tensile strength which was still significantly lower than the base material. However, aging increased the yield strength by ~50 MPa while lowering the ductility by ~6%, producing results equivalent to or higher than the base material in the transverse and short transverse direction. For Part 2 and 3 in the aged condition the yield strength in the short transverse orientation was improved over the base material by 14% and 10% respectively, while ductility showed an improvement of 115% and 137% in the same orientation. Because of a lack of material, the XY direction was not tested in the aged condition

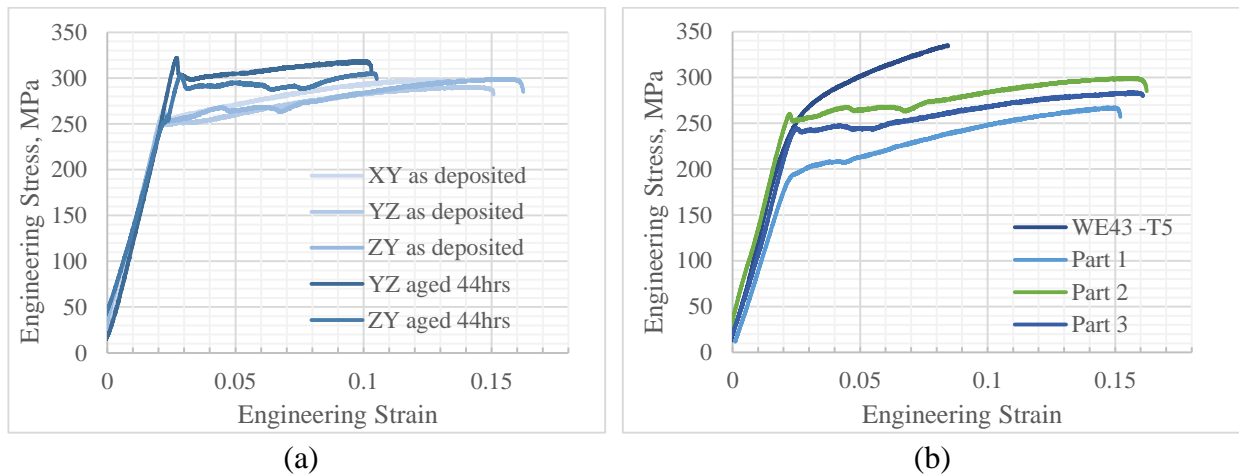


Figure 6: Typical stress-strain curves for (a) different sample orientations of Part 2, and (b) the ZY orientation in the base and Parts 1, 2, and 3 as deposited.

The most isotropic of the samples was Part 2, with the yield and ultimate tensile strengths all within a 10 MPa range and the ductility within a 1.1% range in the as-deposited condition. Representative stress-strain curves for the three orthogonal directions of Part 2 are shown as the three lighter curves in Figure 6a. Isotropy is still maintained in the aged condition, as can be seen by the darker curves in Figure 6a.

The limiting strength factor for the all tested samples was in the ZY direction. Figure 6b shows a representative comparison of these ZY tensile results. There are obvious differences in the shape of the curves for the base and deposited materials. All parts showed higher elongation and lower strain hardening behavior than the base. All parts also displayed yield point elongation which correlated to Luders bands appearing on the samples. There were also differences between the

non-cooled Part 1 and the cooled Part 2 and 3. A more obvious yield point phenomenon appeared on the Parts 2 and 3 while Part 1 had a higher strain hardening rate.

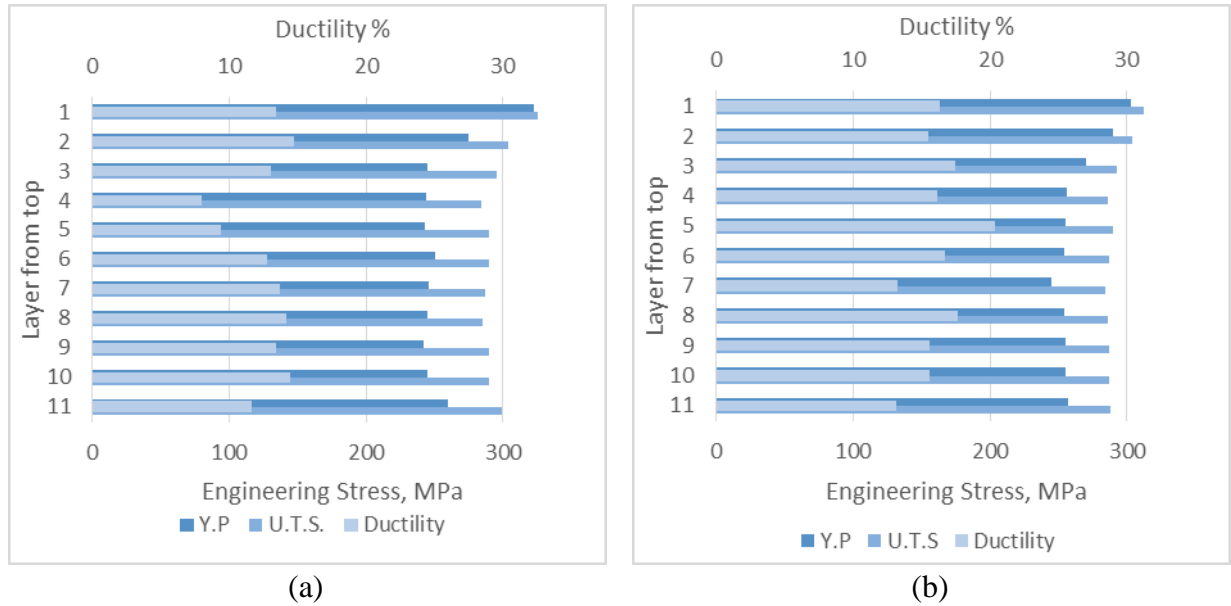


Figure 7: XY tensile results by layer for (a) Part 2 and (b) Part 3

The tensile results show some changes relative to the depth from which they were sampled. Figure 7 shows the XY tensile results by layer sampled from the top, 1, to the bottom, 11, of Part 2 (a) and Part 3 (b). Tensile sample layers (0.06 in) corresponded to two deposited layers (0.03 in). For both XY and YX tests, the highest ultimate strength and yield occurred in the top two layers. The highest overall tensile strength was seen in the top sampled layer of the Part 2 with an ultimate tensile strength and yield of 325 and 323 MPa. The top XY sampled layer also showed no strain hardening behavior. Tensile results from below these two sampled layers tended to be fairly consistent. For this reason, the averages shown in Figure 5 were calculated from the results below layer 2.

Vickers Microhardness Results

Hardness results for the base T5 and as-deposited samples, given in Table 1, are similar to the ultimate tensile strength results. The heat-treated base material had the highest hardness values and Part 2 had the lowest. In their as-deposited state, Part 2 and 3 showed an increase in hardness over the Part 1 but still remained below the average of the base material in the T5 condition.

Table 1: Vickers Microhardness Results

	WE43 T5 condition	Part 1 as deposited	Part 2 as deposited	Part 2 aged	Part 3 as deposited	Part 3 aged
Average	103.0 ± 5.0	73.4 ± 2.0	84.0 ± 3.0	94.4 ± 3.0	85.6 ± 2.7	90.7 ± 3.6

Vickers microhardness profiles for the deposited samples are given in Figure 8. The higher hardness values are experienced in the same areas with the lowest grain sizes and highest tensile

strengths. Part 1 has higher hardness values at its top and bottom. Parts 2 and 3 have their highest values near the top layers with fairly consistent results between the top layers and the substrate. It is also apparent that the heat-treated substrates show some reduction in hardness after exposure to the multiple thermal cycles of the deposition process, dropping from ~103 HV to ~75.

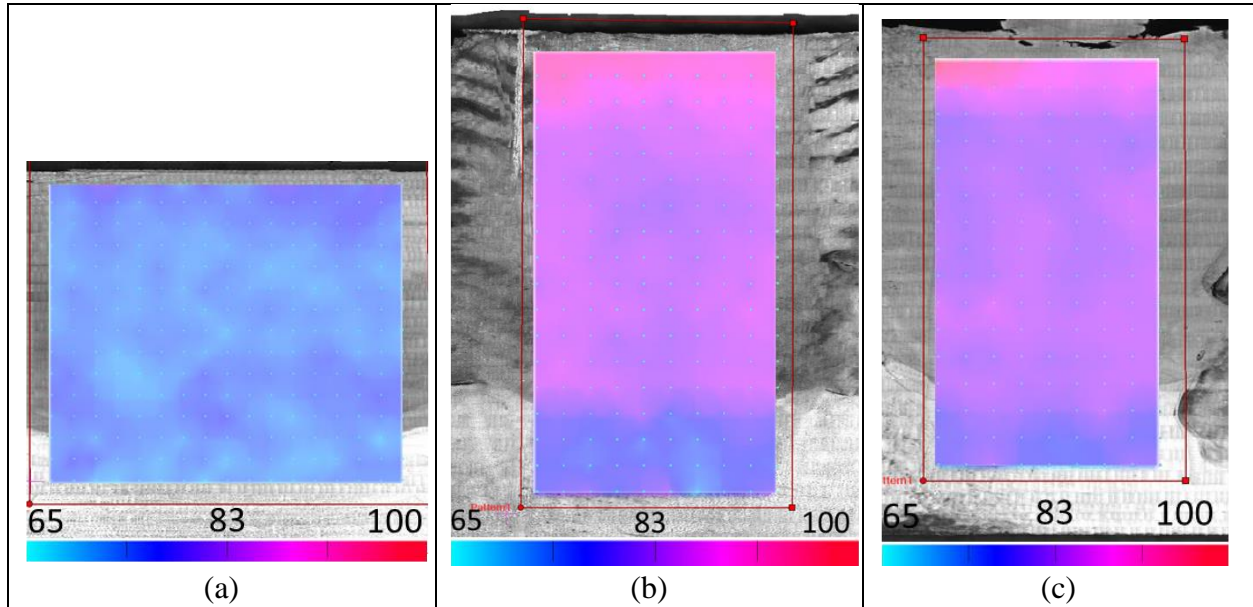


Figure 8: Vickers microhardness profiles of as deposited (a) Part 1, (b) Part 2, and (c) Part 3.

Post deposition heat treatments proved to be an effective way of increasing the hardness of the deposited and substrate material. During the aging process, the substrates of Parts 2 and 3 recovered to an average substrate hardness of 95 HV. As with the tensile tests, Part 2 showed a larger increase in hardness with aging than Part 3. Results after aging are more consistent with the ultimate tensile strength than with the yield strength as the aged results still show a decrease over the base material in the T5 condition.

Charpy Impact Test Results

Average impact results for Parts 1-3 in their as-deposited condition are compared with the WE43-T5 rolled plate in Table 2. The as-deposited samples displayed equal or slightly higher results than the base T5 material, with the most energy being absorbed by Part 2.

Table 2: Charpy Impact Results

	WE43-T5 Rolled Plate	Part 1 as deposited	Part 2 as deposited	Part 3 as deposited
Impact (Joules)	3.8 ± 0.5	3.8 ± 0.6	4.8 ± 0.2	4.5 ± 0.6

Though impact values were similar, the fracture surface topography (Figure 9) varied between sample sets. The WE43-T5 rolled plate samples had a coarser look to their fracture surface, and small cracks could be seen at low magnification (Figure 9a). Part 1 (b) and Part 2 (c) had very

fine homogenous fracture surfaces. The majority of Part 3 surfaces appeared similar to Part 1 and 2, however, there were minor cracks and small clusters that appeared on the surface (d).

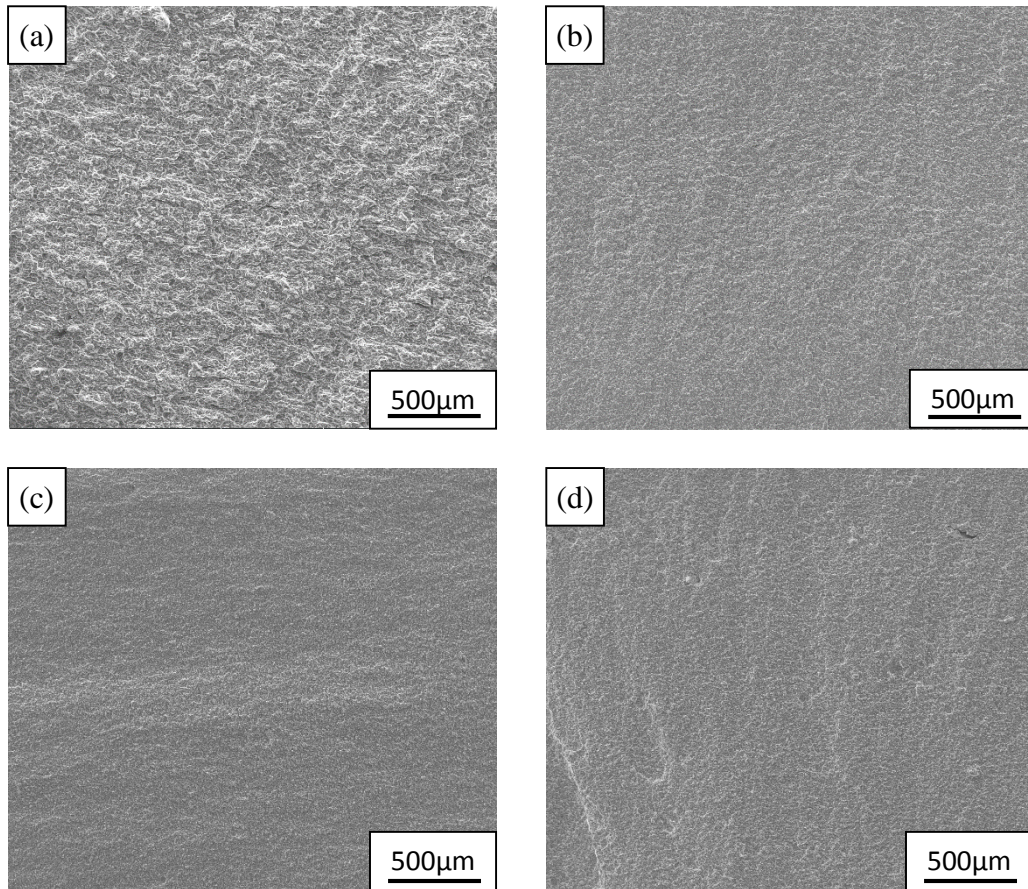


Figure 9: Representative fracture surface topography for (a) WE43-T5 plate, (b) Part 1, (c) Part 2 and (d) Part 3.

The WE43-T5 rolled plate showed signs of brittle and ductile fracture. The fracture surface was fairly smooth and flat, indicating the brittle fracture associated with the low Charpy impact values. However, fractographs like the one shown in Figure 10a, revealed transgranular cleavage along with ductile tears joining cleavage planes. Fine tear ridges and secondary cracks were apparent. Tongues were formed when the cleavage fracture deviated from the cleavage plane and propagated a short distance along a twin orientation. The microstructure at these fracture surfaces, as shown in Figure 10a, showed a similar torn appearance with twinning visible in many of the larger grains.

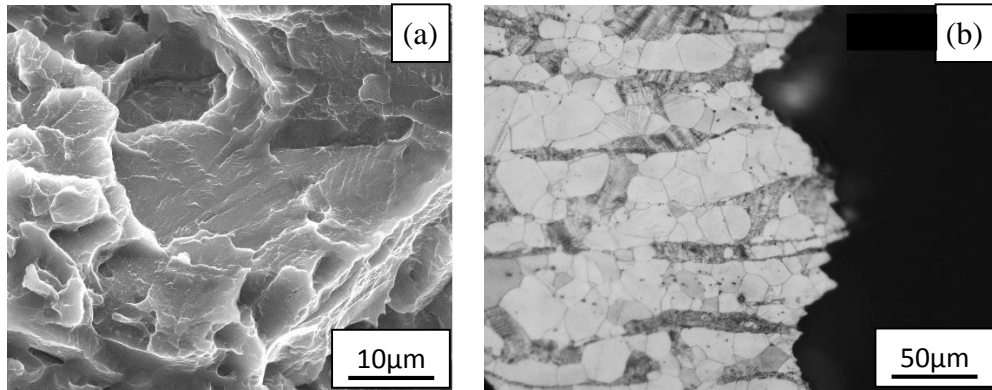


Figure 10: WE43-T5 fractograph (a) and representative microstructure (b) of fracture surface.

The observed fracture surfaces of the Parts 1 and 2 were very similar. Fractographs of Part 1 (Figure 11a) and Part 2 (Figure 11b) revealed evidence of mixed modes of fracture. The fracture surfaces exhibited features whose size corresponded well with the grain size, although there were no clear intergranular facets. The fracture surfaces showed fine transgranular tearing features, but obvious dimples could not be seen either. Charpy Impact fracture surfaces were not distinguishable from those seen in the tensile tests (Figure 11c). Micrographs (Figure 11d) revealed transgranular cleavage similar to the base material, although twins were largely absent near the fracture surface in the comparatively smaller grains of Part 1.

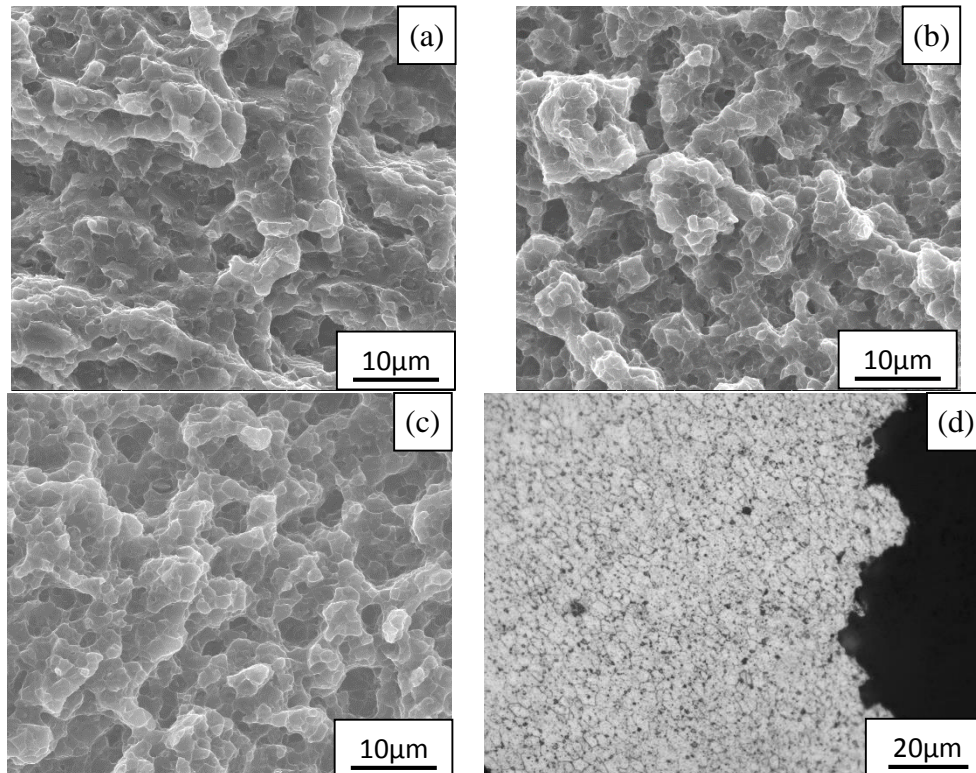


Figure 11: Fractographs from Charpy impact samples of (a) Part 1, (b) Part 2 and from (c) transverse tensile sample of Part 2. Representative microstructure (d) from Part 1.

A representative fractograph of Part 3, as seen in Figure 12a, showed similar signs of a mixed mode of fracture. It also showed evidence of the layers formed during deposition. These layers could be seen in the etched cross section of one Charpy sample, with its macrograph shown in Figure 12b. Some of the brighter locations correspond to bands of larger grains 4 – 6 μm in size, that swept down from one apparent layer towards the one below. Cracks in the sample propagated along these bands, as can be seen in Figure 12c. However, this feature was atypical for fracture surfaces, with most surfaces appearing similar to Parts 1 and 2 as shown in Figure 9d.

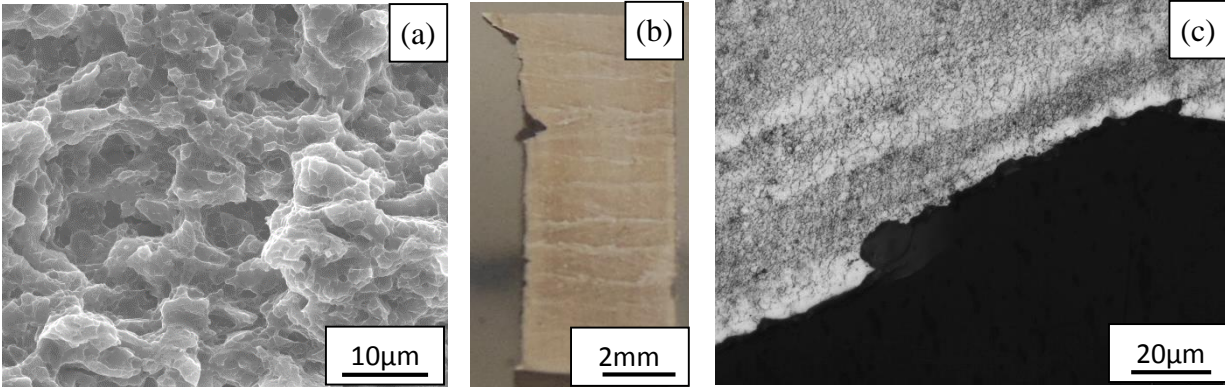


Figure 12: Part 3 Charpy impact sample fractograph (a), macrograph (b), and microstructure (c).

Thermal Profile

The recorded temperature of the bottom of Part 1 is shown in Figure 13. Temperature peaks could be seen when the tool passed over the thermocouple at each of the 24 layers. The maximum temperature recorded was 411 $^{\circ}\text{C}$ (772 $^{\circ}\text{F}$) during the first layer. The temperature profile then showed reductions in peak temperature and increases in minimums over time. Obvious decreases in temperature occurred during the cooling cycles. The maximum temperature observed on the substrate was below the melting range of WE43, which is between 540 and 640 $^{\circ}\text{C}$ (1004 and 1184 $^{\circ}\text{F}$).¹⁶

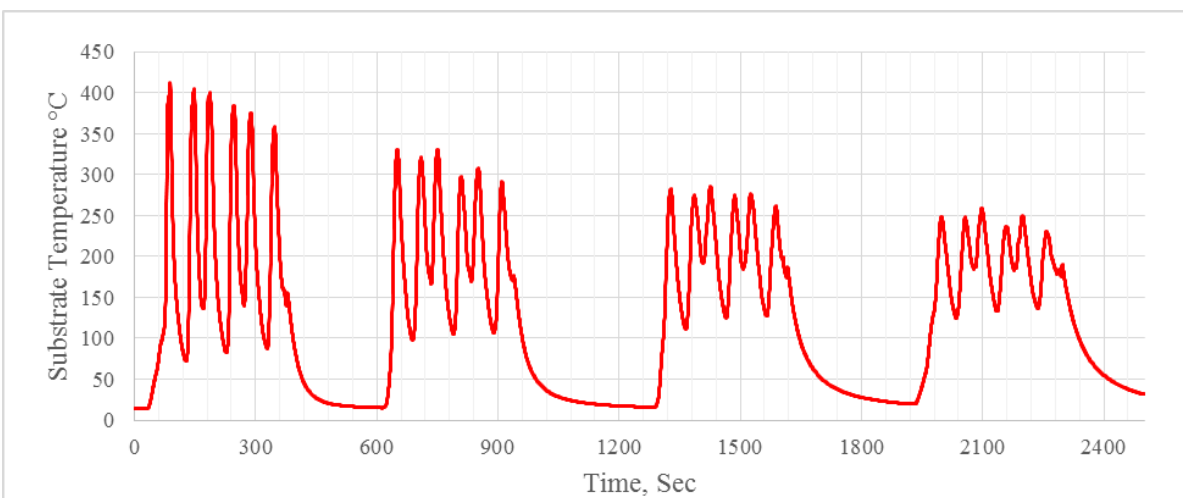


Figure 13: Thermal profile of Part 1 substrate during deposition.

DISCUSSION

The Additive Friction Stir parameters employed in this study produce fully dense, fine grain wrought microstructural parts from WE43 magnesium alloy. Owing to the severe plastic deformation that happened under the added force of the rotating tool and the extruded feed material, parts produced by this method were visually free of voids and interfacial defects between deposited layers. Parts were produced without the need of post processing densification. The parts showed few obvious layers in their microstructure, indicating not only strong bonds between the additive layers but mixing of those layers as well. The strong bonds between the layers, without interfacial defects- AFS to continuously and rapidly build layers without any machining or prepping of the previous layer that can slow down other additive processes.

The microstructural evolution of the parts produced by AFS was clearly affected by the starting microstructure of the feed material, the number of thermal cycles experienced, and by the cooling rate. Results from the top layer indicate that the feed material undergoes grain refinement from severe plastic deformation, which may leave some residual plastic strain in the material as indicated by the higher hardness and higher tensile yield without strain hardening. The next layers indicated annealing as the material was re-heated and underwent further plastic deformation. It is apparent from the rapidly cooled samples, that the microstructure of the filler material as it entered the deposit, as shown in Figure 3b and Figure 4a, played a significant role in the final grain size and distribution. Part 2, with its smaller filler material grain size and distribution, had the smallest final size and distribution as well. Although Part 3 had an overall homogeneous grain structure, there were small local variations in grain size caused by the larger filler material grain size and distribution. Part 1 then, reflected the role that grain coarsening played in the final grain size and distribution. After being initially deposited, the microstructure was then affected by grain growth happening during the thermal cycling from each of the additional layers added. The use of rapid cooling reduced the amount of grain growth by limiting the amount of grain growth after deposition. This resulted in Parts 2 and 3, with rapid cooling, having the smallest grain size range.

It is well known that grain size plays a significant role in the mechanical behavior of materials. Yield strength and hardness have been shown to have an inverse relationship to grain size as predicted by the well-known Hall-Petch^{17,18} equation:

$$\sigma_{0.2} = \sigma_0 + k_y d^{-\frac{1}{2}} \quad (1)$$

Where $\sigma_{0.2}$ is the yield strength, σ_0 is the friction stress, k_y is a material dependent strengthening coefficient and d is the grain size. In the absence of work hardening, $Hv = 3\sigma_{0.2}$.¹⁹ This allows the equation to be re-written with variables suitable for hardness:

$$Hv = H_o + k_h d^{-\frac{1}{2}} \quad (2)$$

Average hardness values for the center and bottom of the depositions along with the top of the substrate at the interface (average grain size of 14.8 μm) were plotted against their reciprocal grain sizes in Figure 14. Fitting to the equation gives values of $H_o = 64$ and k_h as 31.

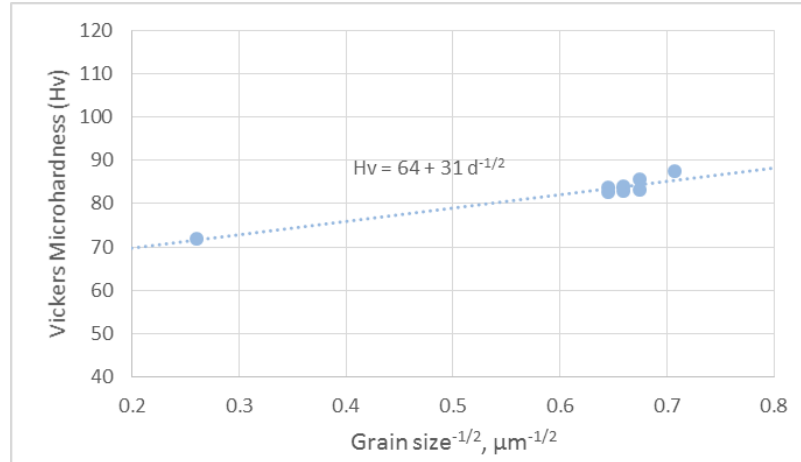


Figure 14: Hall-Petch relationship of deposit and substrate interface.

While comparable data is still lacking in WE43, this compares well with data previously reported on friction stir welded thixomolded AZ91 ($H_o = 64$ and k_h as 27) and rapidly solidified Mg Alloy AZ91 ($H_o = 40$ and k_h as 64).²⁰

The combined results show lower k_h values rates for the friction stir processes relative to grain size. This is likely because the Hall-Petch equation does not take into account second phase particles, precipitates, or a high density of dislocations, which can all slow dislocation movement and lead to higher hardness. High hardness and yield strength in the un-annealed top layers of the deposits was likely due to high densities of dislocations.

The precipitation hardening of WE43 affected the yield and hardness values of the samples. Aging the samples brought about an increase in yield strength and hardness of the depositions and a recovery of hardness in the substrates. This study used only preliminary tests of various heat treatments based on the limited current knowledge of post processing treatments²¹⁻²², more work is needed to determine optimum heat treatments.

In general, the layer by layer approach for the Additive Manufacturing of metals produces microstructural and mechanical property anisotropy²³, with the build direction having the weakest properties.²⁴ This is typically caused by material alignment during processing, defects at layer interfaces, and local changes in thermal history. However, it is clear from the microstructure and mechanical properties of these parts that this generality does not extend to AFS. While there are minor changes from thermal history, all three parts show a high degree of isotropy. With rapid cooling, properties in the build direction meet or exceed those in the longitudinal and transverse directions. Layer effects are not seen in the microstructure, tensile properties, or hardness values. It can also be assumed by the isotropy, that a nearly random texture has been imparted during processing.

AFS is capable of producing magnesium alloys with high amounts of ductility, even in the build direction. This increase in ductility led to an increase in Charpy impact strength.

For large magnesium parts, the AFS process with power feeding provides a continuous process capable of producing high quality parts. However, the rod fed process has the advantage of being

easier to start and stop with only minor decreases in strength, making it ideal for adding small features or doing minor repairs.

CONCLUSIONS

In this study, AFS is shown to be a viable solid-state additive manufacturing method for multi-layered magnesium parts. WE43 atomized powder, and WE43-T5 plate was successfully deposited into a fully dense part with a homogeneous fine grain wrought microstructure without the aid of any secondary densification process. Rapid cooling with liquid nitrogen was able to slow grain growth and reduce the average final grain size to between 2.0 and 2.4 μm .

Mechanical testing of the AFS deposits showed nearly isotropic tensile properties, with impact energy values that were comparable to wrought WE43-T5. Tensile and microhardness results reflected local grain size variation in the deposits due to thermal history

- Atomized powder filler achieved a yield strength of over 207 MPa along with elongation exceeding 10%.
- Atomized powder filler, with rapid cooling, achieved a yield strength over 246 MPa with elongation exceeding 11%.
- With heat treatments, the rapidly cooled powder yield strength was raised to over 302 MPa, with elongation exceeding 7%.
- WE43-T5 rod filler, with rapid cooling, achieved a yield strength over 243 MPa with elongation exceeding 12%.
- With heat treatments, the rapidly cooled rod yield strength was raised to over 281 MPa, with elongation exceeding 10%.

References

1. A. Wrigley, "Magnesium use rising," *Automotive Manufacturing & Production*, 1997, vol. 109, no. 6, pp. 26-27.
2. A. Yamashita, Z. Horita and L. T.G, "Improving the mechanical properties of magnesium and a magnesium alloy through severe plastic deformation," *Materials Science and Engineering*, 2001, vol. A300, pp. 142-147.
3. X. Wang, L. Jin, Y. Li and X. Guo, "Effect of equal channel angular extrusion process on deformation behaviors of mg-3Al-zn alloy," *Material Letters*, 2008, vol. 62, no. 12, pp. 1856-8.
4. J. Bohlen, M. Nürnberg, J. Senn, D. Letzig and S. Agnew, "The texture and anisotropy of magnesium-zinc-rare earth alloy sheets," *Acta Materialia*, 2007 vol. 55, no. 6, p. 2101-2112.
5. F. Czerwinski, *Magnesium Injection Molding*, New York: Springer, 2008.
6. G. Lorimer, L. Mackenzie, F. Humphreys and T. Wilks, "The Recrystallization Behavior of AZ31 and WE43," *Materials Science Forum*, 2005, Vols. 488-489, pp. 99-102.
7. E. Aghion, Y. Gueta, N. Moscovitch and B. Bronfin, "Effect of yttrium additions on the properties of grain-refined Mg-3% Nd alloy," *Journal of Materials Science*, 2008, vol. 43, pp. 4870-4875.
8. Y. Kang, D. Wu and R. H. E. Chen, "Microstructures and mechanical properties of the age hardened Mg-4.2Y-2.5Nd-1Gd-0.6Zr (WE43) microalloyed with Zn," *Journal of Magnesium and Alloys*, 2014, vol. 2, pp. 109-115.
9. T. Mohri, M. Mabuchi, N. Saito and M Nakamura, "Microstructure and mechanical properties of a Mg-4Y-3RE alloy processed by thermo-mechanical treatment," *Materials Science and Engineering*, 1998, vol. A257, pp. 287-294.
10. S. Yang and B Zhang, "Experimental study of electron beam welding of magnesium alloys", *Rare Metals*, 2011, vol. 30, pp. 364-369
11. C.C. Ng, M.M. Savalani, M.L. Lau and H.C. Man, "Microstructure and mechanical properties of selective laser melted magnesium," *Applied Surface Science*, 2011, vol. 257, pp. 7447-7454
12. C. Bettles, "Magnesium Powder Metallurgy: Process and Materials Opportunities," *Journal of Materials Engineering and Performance*, 2008, vol 17, no. 3, pp 297-301
13. H. T. Fujii, M.R. Spiraman and S.S. Babu, "Quantitative Evaluation of Bulk and Interface Microstructures in Al-3003 Alloy Builds Made by Very High Power Ultrasonic Additive Manufacturing" *Metallurgical and Materials Transactions*, 2011, vol 42A, pp 4045-4055.
14. S. Palanivel, P. Nelaturu, B. Glass and R. Mishra, "Friction stir additive manufacturing for high structural performance through microstructural control in an Mg based WE43 alloy," *Materials and Design*, 2015, vol. 65, pp. 934-952.
15. R. Mishra and Z. Ma, "Friction stir welding and processing," *Material Science and Engineering*, 2005, vol. R, no. 50, pp. 1-78.
16. Magnesium Elektron, *Elektron WE43 datasheet 467*, Madison, IL: Magnesium Elektron Ltd, 2014.
17. E.O. Hall, "The Deformation and Ageing of Mild Steel: III Discussion of Results," *Proceedings of the Physical Society*, 1951, Vol 64, pp 747 - 753.
18. N.J. Petch, "The cleavage strength of polycrystals", *J. Iron Steel Inst.*, 1953, vol 173, pp. 25-28.
19. M.F. Ashby, D.R.H. Jones, *Engineering Materials 1: an introduction to properties, applications, and design (4th)*, Elsevier, Oxford, 2012, p. 160-161.
20. S.H.C. Park, Y.S. Sato and H. Kokawa, "Microstructural evolution and its effect on Hall-Petch relationship in friction stir welding of thixomolded Mg alloy AZ91D," *Journal of Materials Science*, 2003, vol 38, pp. 4379 - 4383
21. P. Mengucci, G. Barucca, G. Riontino, D. Lussana, M. Massazza, R. Ferragut and E. Hassan Aly, "Structure evolution of a WE43 Mg alloy submitted to different thermal treatments" *Material Science and Engineering*, 2008, vol. 479, pp 37-44.
22. S K. Panigrahi, R S. Mishra, K. Kumar, R. Delorme, B. Davies, R A. Howell and K Cho, K "A Study on Combined Effect of Forging and Ageing in Mg-Y-RE Magnesium Alloy," *Minerals, Metals and Materials Society/AIME*, Feb. 2001

23. O. Ivanova, C. Williams and T. Cambell, "Additive manufacturing (AM) and nanotechnology: promises and challenges" *Rapid Prototyping Journal*, 2013, vol. 19.5, pp 353-364.
24. W. Frazier, "Metal Additive Manufacturing," *Journal of Materials Engineering and Performance*, 2014, vol. 23, pp. 1917-1927.